JOURNAL OF GEOPHYSICAL RESEARCH, VOL. 103, NO. A4, PAGES 6771–6784, APRIL 1, 1998

Numerical simulation of VLF risers, fallers, and hooks observed in Antarctica

A. J. Smith
British Antarctic Survey, Cambridge, England

D. Nunn
Department of Electronics and Computer Science, Southampton University
Southampton, England

Abstract. The VLF database from Halley station, Antarctica, has been searched, and prominent examples of discrete emissions are presented. Risers, fallers, quasi-constant tones, and upward and downward hooks are all common. Also observed are risers and fallers triggered from the tops of hiss bands. A one-dimensional Vlasov VHS code has been used to simulate the main types of events observed. Using realistic plasma parameters, the code successfully reproduces the main kinds of events observed, in good qualitative agreement with observations. Distinct generation region structures are found to be associated with risers and fallers. Hook formation is interpreted as being a spontaneous transition between these two quasi-stable generation region structures.

1. Introduction

Discrete narrowband or band-limited whistler mode emissions have been observed for many years, both on the ground [*Helliwell,* 1983, 1988] and in space [*Burtis and Helliwell,* 1976; *Nagano et al.,* 1996; *Nunn et al.,* 1997]. Discrete VLF emissions are observed in the Earth's magnetosphere over a wide range of L values, from $L = 2.5$ out to the dayside magnetopause at $L = 10$. Observationally, discrete VLF emissions are characterized by their large amplitude and self-sustaining nature. The most outstanding feature of VLF emissions is their sweeping frequency. Emissions may be broadly categorized by their spectral shape $f(t)$. The most common form is that of the pure riser, where frequency sweep rates in the range 300–1000 Hz s^{-1} are the norm and the total frequency change between the start and the end of an emission may be of the order of 100–2000 Hz [see *Helliwell,* 1965]. The second most common emission type is the falling tone, which is often observed to be highly monochromatic and triggered off the end of a transmitted pulse [*Helliwell and Katsufrakis,* 1974]. A third type often seen is the hook-shaped emission, which may be either upward or downward. At Halley station, Antarctica, long enduring zigzag emissions, composed of alternating upward and downward hooks, are sometimes seen. VLF emissions may also be characterized by their trigger source. The first observed VLF emissions were triggered by CW pulses from terrestrial VLF transmitters [*Helliwell,* 1965]. Emissions are also observed to be triggered from the tops of hiss bands, by power line harmonic radiation (PLHR), and by lightning whistlers [*Nunn and Smith,* 1996]. It is an important observational feature that strong VLF emissions may be triggered by very weak signals. Indeed the trigger source may be invisible. Such apparently spontaneous emissions are very common and usually referred to as discrete emissions.

The process by which triggered VLF emissions are produced is a fascinating and important problem in theoretical plasma physics. As a result of the narrow bandwidth and distinctive spectral shape of VLF emissions, this is a very clear-cut and well-defined problem that is amenable to theoretical investigation and numerical simulation. In a previous paper [*Nunn and Smith,* 1996] we described a set of typical observations of VLF emissions triggered by lightning whistlers, as observed at Halley. We reported simulations of these events, using a one-dimensional Vlasov (VHS) code. The simulations assumed that there were parallel propagating whistler waves and that the wave amplitudes were large enough ($\geq$4 pT) to cause nonlinear trapping of cyclotron resonant electrons in the equatorial zone. Under these assumptions the code seemed to be successful in simulating the observed characteristics of observed whistler-triggered emissions. In this paper we describe a much improved version of the VHS/VLF code and its application to the simulation of risers, fallers, and hooks observed at Halley. We shall concentrate on discrete emissions with no obvious trigger source, and also on risers and fallers triggered by hiss bands.

Paper number 97JA03396.
0148-0227/98/97JA-03396$09.00

2. Data

The observational database of VLF emissions, used in this study for evaluating the results of the simulations, was described in some detail by *Nunn and Smith* [1996] and will only be summarized here.

British Antarctic Survey has an extensive collection of ELF/VLF broadband (0.5–10 kHz) radiowave data from its Antarctic research stations Halley (76°S, 26°W) and Faraday (65°S, 64°W), dating from 1967. The waveforms of the horizontal magnetic components of the wave field at the ground have been recorded on analog and, more recently, digital tape. For more details of the receiving and recording systems, refer to *Yearby and Smith* [1994] and *Smith* [1995]. The data are analyzed by playing back the data tapes through the Advanced VLF Data Analysis System (AVDAS) [*Smith et al.*, 1994], a real time interactive spectrum analyzer.

In this paper we use only recent data from Halley, which is situated close to the $L = 4$ shell. Figure 1 illustrates typical examples of the risers, fallers, and hooks which we later attempt to simulate. All the examples are presented in the form of spectrograms, produced by the AVDAS, in which frequency and time are the ordinate and abscissa and spectral intensity (expressed in decibels relative to a reference of 10^{-33} T^2 Hz^{-1}) is represented by the grey scale.

Figure 1a shows a sequence of risers, which characteristically begin near a constant frequency, in this case 1.8 kHz. (It has been suggested [*Park*, 1977] that this common starting frequency is due to a coherent power line harmonic that is too weak to be directly observed.) They rise in frequency, slowly at first, then with df/dt increasing to about 1500 Hz s^{-1}. As they rise in frequency, the amplitude also initially increases but then decreases again, until the riser is cut off at a frequency that varies from event to event but in this case is in the range 3.0–3.5 kHz. The end of some of the risers is marked by the triggering of a faller rather than a complete cutoff. Just before the riser cutoff the rate of frequency rise, df/dt, also has a tendency to decrease. Note that because of whistler mode dispersion between the source region (usually assumed to be near the equatorial plane) and the ground, the riser f–t profile as it leaves the source region will be slightly different from what is observed on the ground.

In Figure 1b a faller begins near 1744:32.0 UT at ~2.7 kHz and falls to ~1.7 kHz with a steady df/dt value of ~−1000 Hz s^{-1}. Figure 1c shows a more complex example. In the first half of the frame there are a couple of risers similar to those of Figure 1a. Superimposed is a discrete emission which appears to vary quasi-sinusoidally in frequency about 2.6 kHz before ending in a downward hook (turning point at 1734:38 UT). The event shown in Figure 1d is an almost exact inverse of the preceding example, i.e., an upward hook; the rate of change of frequency and cutoff at the end of the emission are of similar order of magnitude to the risers of Figure 1a.

Figure 1e is again somewhat complex. A series of linked risers and fallers in the first part of the frame combine to form an emission with a quasi-sinusoidally varying frequency. At 1250:12 UT a whistler is seen, followed by a short riser spanning $f = 4.0$–4.7 kHz, and a separate hook. It is possible, though not certain, that these were triggered by the whistler. At $t \simeq 2.8$ s, a narrow faller grows in the weak hiss band and then falls below it. A second, even weaker, hiss band appears to provide the starting point for a different series of fallers.

In Figure 1f a faller emerges from the bottom of a hiss band, while in Figure 1g a series of risers originate near the top of one. The example of Figure 1h is similar to that of Figure 1c. A discrete emission with fluctuating frequency, this time occurring along the top of a hiss band, terminates in a strong downward hook, which drives right through the hiss band.

3. Simulation Code

The code simulates numerically the self-consistent nonlinear cyclotron resonant interaction between a band-limited VLF wave field and a "hot" anisotropic distribution of electrons. The spatial domain of the simulation is in the equatorial region, where nonlinear trapping is possible and the resonant energy is lowest. The code is 1-D and assumes propagation parallel to the ambient field (coordinate z). Note that it reproduces exactly linear behavior in the low-amplitude regime—indeed in this case, code output will be fairly precise, since nearly all the approximations in the code appertain to the nonlinear case.

The code employs a simulation technique called Vlasov Hybrid Simulation (VHS), which is well suited to the problem at hand. In this paper, only a general discussion of the code will be given. Mathematical details can be found in the paper by *Nunn* [1990]. *Nunn* [1993] describes the VHS method in very general terms, *Nunn and Smith* [1996] describe recent updates and give simulations of whistler-triggered emissions, and *Nunn et al.* [1997] present simulations of VLF emissions and chorus observed on the Geotail satellite at $L = 10$.

3.1. Field Equation

Since the simulation is band limited, the code defines a base frequency ω_0 and base wave number $k_0(z)$. This fast phase variation is divided out, allowing us to define a complex dimensionless amplitude $\tilde{R}(z,t)$ and the corresponding dimensionless resonant particle current $\tilde{J}(z,t)$. The dimensionless analysis uses $1/\bar{k}$ as the unit of length, where $\bar{k} = \Pi_e/c$, and $1/\bar{\omega}$ as the unit of time, where $\bar{\omega} = \Omega_e/2$, and Π_e and Ω_e are the local plasma frequency and local electron gyrofrequency, respectively.

Under the assumption that $\tilde{R}(z,t)$ is slowly varying (narrowband approximation), Maxwell's equations and

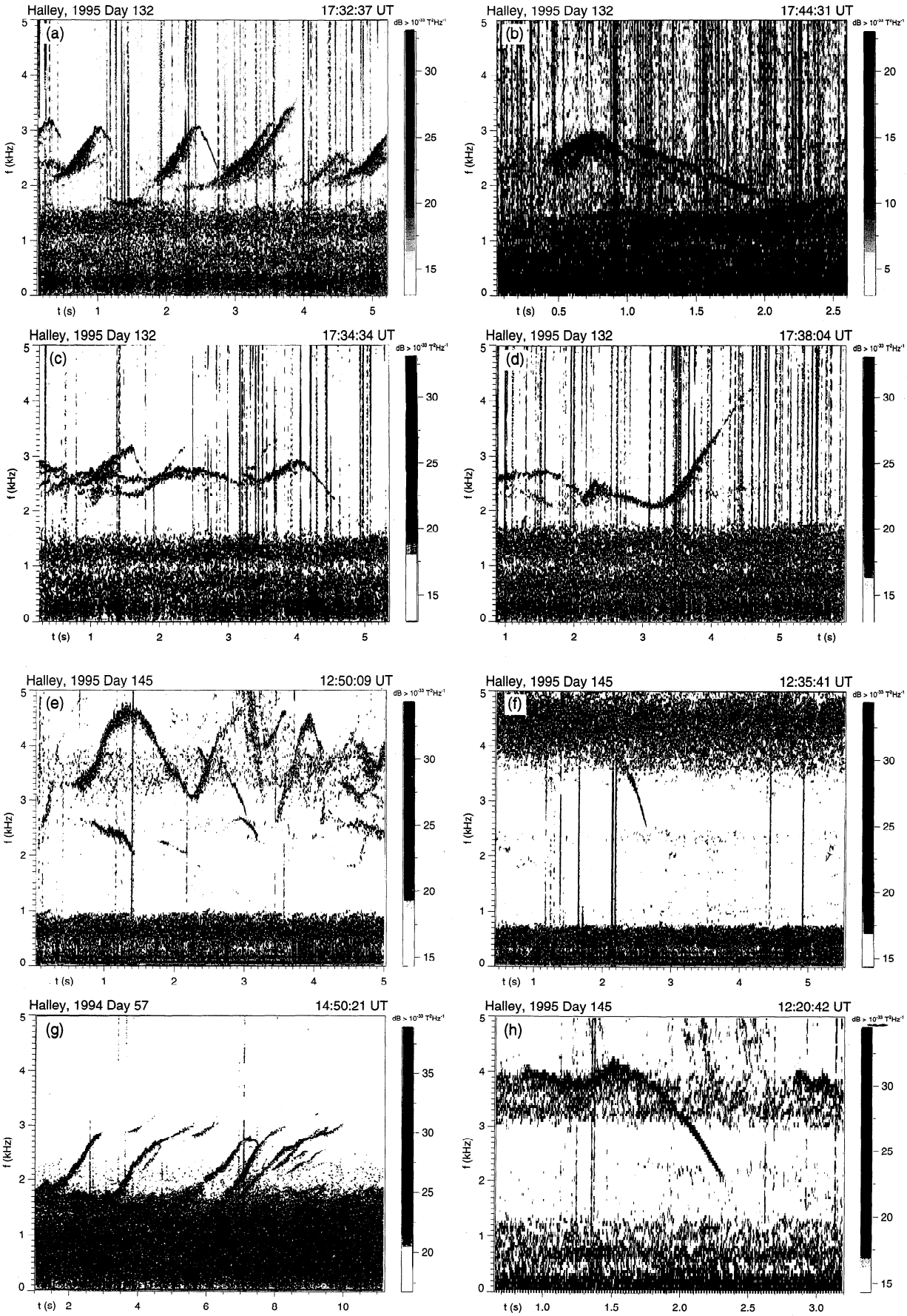

Figure 1. (a)–(h). Grey scale 0–5 kHz spectrograms of typical risers, fallers, and hooks observed at Halley during 1994–1995. The timescales show seconds relative to the UT shown at the top right of each spectrogram. See text for description of the phenomena.

the linear equations of motion of the cold plasma furnish the field equation

$$\left(\frac{\partial}{\partial t}+V_g\frac{\partial}{\partial z}\right)\tilde{R}=-\frac{\omega_o V_g}{k_0}\tilde{J}-\gamma_{NL}(|\tilde{R}|)\tilde{R} \quad (1)$$

Note that for VLF emission simulations the average frequency changes over a wide range. During the simulation the base frequency is continually redefined.

The ambient magnetic field is assumed to have a parabolic dependence on z,

$$B_0(z)=B_0(0)(1+0.5\chi z^2) \quad (2)$$

with a scale factor χ appropriate to $L=4.3$. Variations in χ are not critical, nor are departures from exact parabolicity.

3.2. Saturation Mechanism

In simulating VLF emissions we are dealing with a plasma that is absolutely unstable in the nonlinear regime. For a 1-D code with a parabolic inhomogeneity there is nothing to limit the growth of the wave field. This situation is different from the homogeneous problem, where nonlinear trapping limits growth. For a 1-D code it is necessary to insert amplitude saturation phenomenologically. The most likely physical mechanism is as follows. The nonlinear current $\tilde{J}$ is actually three-dimensional and on wave number decomposition will be found to radiate into a broad spectrum of wave numbers. Energy radiated into nonparallel directions will propagate laterally away from the generation region and be Landau damped, thus providing a mechanism for power loss. Another physical mechanism will also be operative. Nonlinear trapping in inhomogeneous media generates a hole (or a hill) in the phase-averaged distribution function. Electrostatic waves with phase velocities on the upper side of a hole or lower side of a hill will experience large linear Landau growth rates. The resulting electrostatic wave field will quench gradients in the V_z direction and thus reduce cyclotron growth rates. Neither mechanism is understood at present, and both require simulations with complex 3-D codes currently beyond the reach of computer technology.

The saturation term $-\gamma_{NL}\tilde{R}$ is shown in (1) as an extra damping term. The nonlinear damping rate γ_{NL} increases rapidly above some level $|\tilde{R}|>R_{max}$, normally chosen to fit observed amplitudes. Even if γ_{NL} is a function of a weighted average of $|\tilde{R}|$ over the whole z domain, this saturation mechanism will bias the spectrum, tending to broaden and flatten it. An alternative approach is to employ a nonlinear loss term, applied in the Fourier domain. If $\{R_k\}=\mathrm{FFT}\{\tilde{R}(z_i)\}$ is the spatial fast Fourier transform (FFT) of the $\tilde{R}$ field on the z grid, we can update the spatial spectrum R_k at each time step by

$$R_k'=R_k-\gamma_{lin}\Delta t\,U(\bar{R})G(|R_k|) \quad (3)$$

where γ_{lin} is the linear growth rate at the equator $z=0$, $U(\bar{R})$ is a function of global average wave amplitude $\bar{R}$ that rises steeply for $\bar{R}>R_{max}$, and $G(|R_k|)$ is a function that biases the spectrum. This is a fairly general loss mechanism, but it was found that the results using this were little different from those obtained by using (1). It appears that the exact details of the saturation mechanism are unimportant. For weaker linear growth rates it is possible to run the code and trigger emissions, without invoking the saturation mechanism. All "strong" triggering effects do require, however, a sink for wave energy if the process is to be visualized as being one-dimensional.

Carlson et al. [1990] reported on a numerical simulation of electron cyclotron wave-particle interactions for a whistler wave field in a parabolic B field inhomogeneity. The simulations used a zeroth-order distribution function that was either a delta function in parallel velocity or a triangular function centered on the local resonance velocity. They reported a noticeable saturation effect taking place, a different result from ours. This would appear to be due to the rather different nature of their particle excitation.

3.3. Ambient Plasma

The low-energy electron plasma (<50 eV) is linear and for modeling purposes can be represented as being a cold plasma, density $N_e(z)$. The dependence of $N_e(z)$ upon z is not critical but is here assumed to be parabolic:

$$N_e(z)=N_e(0)(1+0.5\nu\chi z^2) \quad (4)$$

Ions are assumed to be immobile. A choice of $\nu=0.3$ is used in these simulations.

The unperturbed hot electron distribution function is specified in dimensionless units by $F_0(\mu,W)$, where W is energy and μ is magnetic moment. Note that all distribution functions in this paper are defined with respect to linear $(\mathbf{r},\mathbf{v})$ phase space; the above F_0 is not particle density in μ,W space! The free energy for the instability must derive from the anisotropy of F_0. To simulate emissions/chorus, we require a linearly unstable plasma and a positive linear growth rate, since nonlinear and linear growth rates are normally of the same sign—nonlinear growth rates being typically larger by a factor of say ~2–5.

The main task of the code is to compute the nonlinear resonant particle current $\tilde{J}(z,t)$, which is the source current or "antenna" in the field equation and generates the emission. If we make the valid assumption that ΔW is small, the formal expression for $\tilde{J}$ is, in dimensionless units,

$$\tilde{J}(z,t)=\frac{2\bar{k}^3}{N_e}\int_{|V_\perp|}\int_{\psi}\int_{V^*}e^{i\psi}\Delta W F_0'|V_\perp|^2 dV^* d\psi d|V_\perp| \quad (5)$$

where

$$F_0'=\left\{\left.\frac{\partial F_0}{\partial W}\right|_\mu+\frac{2}{\omega}\left.\frac{\partial F_0}{\partial \mu}\right|_W\right\}_{V_z=V_{res}} \quad (6)$$

The quantity ΔW is the integrated energy change of a test particle at that point in phase space. The variable ψ is gyrophase, and $V^* = V(z) - V_{\rm res}(0)$ is parallel velocity about resonance. The V^* integral must be evaluated for a narrow range centered on the cyclotron resonance velocity $V_{\rm res}(z,t)$ at the center frequency of the local wave field. It is seen that the driver for the instability is the gradient term $F_0'(|V_\perp|, f(z,t), z)$, which can be viewed as a function of $(z, |V_\perp|)$ and local mean frequency $f(z,t)$. A specific emission event is driven by positive gradients F_0' in a restricted region of velocity space, corresponding to the appropriate range of resonant velocities.

3.4. Frequency Sweep Rate Mechanism

The code will be found to simulate the sweeping frequency of VLF emissions. How does this sweeping frequency come about? If we define $\tilde{R} = Re^{j\phi}$, then ϕ is the additional phase over the base phase. Some manipulation [*Nunn*, 1990] of (1) gives the result

$$\frac{\partial \omega}{\partial t} = \frac{\partial^2 \phi}{\partial t^2} = V_{\rm g}\frac{\partial^2 \phi}{\partial t^2} + \frac{V_{\rm g}^2 \omega_0}{k_0}\frac{\partial}{\partial z}\left(\frac{J_{\rm i}}{R}\right) - \frac{V_{\rm g}\omega_0}{k_0}\frac{\partial}{\partial t}\left(\frac{J_{\rm i}}{R}\right) \tag{7}$$

where $J_{\rm i}$ is the component of $\tilde{J}$ parallel to the local wave $B_\perp$ field. *Helliwell* [1967] and *Carlson et al.* [1985] produced phenomenological theories relating frequency sweep rate to the physical location of the generation region, such that the latter was in a position of zero net inhomogeneity. These theories, although useful and important, never elucidated the mechanism whereby wave phase was actually changed by the resonant particle current. First, the frequency shift mechanism must be nonlinear, and a self-consistent solution of the wave equation is necessary to establish the frequency shift unambiguously. However, a glance at this equation tells us where the shift comes from. The last term cannot give shifts of more than a few hertz. The driver term is the second one, which results from a wave number shift between the nonlinear resonant particle current and the wave field. It is well known that nonlinear trapping in parabolic inhomogeneities can result in a significant value for the global average of $\Phi = \partial/\partial z(J_{\rm i}/R)$. For a VLF emission generation region confined mainly to the region downstream of the equator, with parameters appropriate for $L = 4$, a positive value of $df/dt \sim +200$ Hz s^{-1} would be the best that could be achieved. For a generation region profile extending well upstream of the equator a value of approximately -200 Hz s^{-1} is typical.

Past experience with the code suggests that observed sweep rates of $\sim$kHz s^{-1} can be achieved only if the first term, which is purely advective, is significant. The changing frequency at a fixed point in space is then due to a spatial gradient in wave number. To achieve sweep rates with an advective term may appear underhand. However, a strongly nonlinear $\tilde{J}$ is required to (1) establish a generation region with a wave number gradient across it and (2) maintain it in a constant position on the field line. *Nunn* [1984] studies self-consistent generation regions of VLF emissions that are amenable to modeling. However, the setup process is dynamic, very complex, and only accessible by simulation. It is clear that the quantity $\partial\Phi/\partial z$ is mainly instrumental in setting up such wave number gradients.

3.5. Filtering of the Simulation Field

At each time step the field values on the z grid $\{\tilde{R}(z_n)\}$ must be spatially bandpass filtered to the simulation bandwidth $\sim$33 Hz, which amply covers experimentally observed bandwidths. To allow the center frequency of the band to be a function of z, we employ the following filtering procedure. At each time step t_n the local center wave number $k(t_n, z)$ is estimated. A function $k_m(z)$, which is a polynomial in z of order m, is defined, and a least mean squares fit to k is found. A matched filter is employed as follows [see *Nunn and Smith*, 1996]. The phase variation due to $k_m(z)$ is divided out from $\tilde{R}(z)$, and then $\tilde{R}$ is band-pass filtered to ± 40 Hz by using a spatial FFT and inverse FFT of $\{\tilde{R}(z_n)\}$. The phase variation due to $k_m(z)$ is then added back into $\tilde{R}$. Of course, spatial gradients in frequency/wave number could be accommodated by a much larger overall simulation bandwidth of $\sim$350 Hz. However, since the code run time goes as bandwidth cubed, this option is out of the question. In addition, to assure simulation stability, the wave field is subjected at every time step to a global band-pass filtering operation with a width of the order of 900 Hz.

3.6. Vlasov Hybrid Simulation Method

A 4-D phase box is defined in the variables $z, |V_\perp|, \psi$, and $V^* = V(z) - V_{\rm res}(0)$. The box range in z is fixed from z_l to z_r, where z_r is positive and is on the wave exit side. The box size in z is chosen to be the smaller of the following: (1) the zone of nonlinear trapping, assuming $R = R_{\rm max}$, or (2) the region where the linear growth rate is greater than 0.05 times the equatorial value. In the present simulations, size 1 is usually smaller. The z grid contains $N_z = 1024$ points. The variable ψ is gyrophase and is represented by 20 discrete grid values.

The range in parallel velocity V^*, $V_1^* \rightarrow V_2^*$ spanned by the phase box is a function of z and t and is centered on the local resonance velocity $V_{\rm res}(z,t)$. The width $V_2^* - V_1^*$ covers the range of resonance velocities for the simulation bandwidth, plus three nonlinear trapping widths. The number of grid points in V^* is $N_{V^*} = 40$. Through the variable V^* the phase box is a function of time and matched to the local field in space and time.

The coordinate $|V_\perp|$ is relatively insensitive in this problem. The contribution to current $\tilde{J}$ from each discrete value of $|V_\perp|$ is calculated entirely separately in this code. The range of $V_\perp$ values required in the simulation is quite narrow, corresponding to a pitch angle range of 40°–65°. Low pitch angle particle equations of

motion are linear, and the numbers of particles at very high pitch angles is small. The production runs in this paper will be done with four values of $|V_\perp|$. Enough grid points are needed to resolve the functional dependence of F_0' on $|V_\perp|$. It is also necessary to have enough grid points to span the whole range of $|V_\perp|$ where F_0' is significant, in order for there to be a range of trapping frequencies present and thus to reproduce the sideband stability characteristics correctly.

The main task of the code is to calculate the current $\tilde{J}$ from (5) by using the VHS algorithm. The main features of the algorithm are as follows:

1. At time $t = 0$ the phase box is filled with particles with a density of about 1.2 per grid hypercube.

2. The code follows each particle's trajectory in the phase box. Each particle is embedded in the Vlasov fluid. The whole method is based upon the integral form of the Vlasov equation or Liouville's theorem. The well-known Vlasov codes of *Cheng and Knorr* [1976] and *Denavit* [1972] integrate the Vlasov equation directly, a procedure that requires smoothing of the distribution function, since derivatives in velocity space are involved. Liouville's theorem tells us that F is conserved along these phase trajectories, but the code actually computes ΔW (effectively ΔF) along each trajectory. What the code is essentially doing is computing a large number of continuous phase space trajectories within the phase space box and at each time step interpolating F from the trajectories onto the phase space grid.

3. At each time step, ΔW is interpolated from the particles to the phase space grid by using the following algorithm:

$$\Delta \mathcal{W}_{ijk} = (\sum_{\ell} \Delta W_\ell \alpha_\ell)/(\sum_{\ell} \alpha_\ell) \tag{8}$$

where the sum ℓ is over all particles in cells adjacent to grid point ijk, ΔW_ℓ is ΔW for the ℓth particle, $\Delta \mathcal{W}_{ijk}$ is the value at grid point ijk, and the α_ℓ are area or volume weighting coefficients. The density of the simulation particles themselves is conserved along a phase trajectory, and there is no tendency for them to bunch in phase space. This density must be held above a certain minimum value in order for the interpolation procedure to work. Any density above this floor is permissible, and particles may be inserted into the phase fluid or removed at will. This feature is not shared by any other simulation method.

4. With $\Delta \mathcal{W}_{ijk}$ now defined on the grid, the integral for $\tilde{J}$ in (5) is readily evaluated.

5. Particles leaving the phase box (relative to coordinate V^*) are nonresonant with the local wave field and are discarded from the simulation. New particles have to be inserted into the phase fluid on the edge of the box where phase fluid is flowing in. This operation requires some care.

6. The unperturbed distribution function F_0 is introduced at $z = z_r$, and the wave field exiting the box at $z = z_r$ is collected up into an array for graphical processing.

The VHS method is very suitable for the VLF emission problem where the resonance velocity changes drastically with position and time. Vlasov methods generally are low noise, particularly when $\Delta F \ll F$, since it is effectively ΔF that is pushed. Particle-in-cell (PIC) methods can be used for VLF wave-particle interaction simulations, but they are best for situations where the frequency does not change greatly. They have the advantage that nonresonant particles are not discarded, and thus PIC codes can look at particle diffusion and, given enough computer time, can recirculate particles after two bounces [*Omura and Matsumoto*, 1982, 1985].

4. Simulation results

We now present results from four simulation runs of the 1-D Vlasov VHS code. Our aim is to reproduce the dominant features of the data examples shown. In view of the lack of information on plasma conditions at the emission generation region site there is little point in attempting to produce exact simulations of individual events. Instead we shall aim to simulate qualitatively the main types of triggering behaviors observed.

A number of parameters will be common to all four runs. The exact L shell value for a discrete emission event is hard to infer from the data, even when a nose whistler is present in the same data segment. In these runs we shall assume an L value of $L = 4.3$. The electron gyrofrequency will be taken to be 9 kHz in all cases. The variation of field strength $B_0(z)$ is assumed to be a parabolic function of z (2), with a scale factor χ chosen to correspond to $L = 4.3$. The equatorial cold plasma density N_e is taken to be 380 cm^{-3}, where the z dependence of $N_e(z)$ is also parabolic (4) with the factor $\mu = 0.3$.

The phase space simulation box has $N_z = 1024$ grid points in the spatial variable z, $N_{V^*} = 40$ grid points in parallel velocity, and $N_\psi = 20$ grid points in gyrophase. The number of discrete values of $V_\perp$ considered in the code is either $N_{V_\perp} = 4$ or in some cases $N_{V_\perp} = 1$. The total number of simulation particles at any one time is variable but will be about 1 or 4 million depending on the value of $N_{V_\perp}$.

The choice for distribution function $F_0(\mu, W)$ is not unduly critical in this problem. The distribution function must be anisotropic and linearly unstable to parallel propagating whistler waves over the range of frequencies appropriate to the event in question. The key simulation parameter is the linear cyclotron growth rate at the equator at the simulation starting frequency. The functional dependence of linear growth rate upon frequency controls the progress of an emission with a sweeping frequency, as well as the spatial structure of the emission-generating region. Generally speaking, the nonlinear growth rates will have the same sign as that of the linear growth rate, will be somewhat larger than the

linear growth rate, and will be an increasing function of amplitude.

Nonlinear resonant particle trapping is most prominent in a pitch angle range of 45°–65°. It is therefore necessary to choose a distribution function F_0 that has gradients in velocity space favorable for instability within this pitch angle range and spread over a range of V_z appropriate to the entire frequency range of the emission being simulated. In this paper we shall employ a fairly general model for F_0, which consists of a superposition of five bi-Maxwellian functions,

$$F_0(\mu, W) = \sum_{l=1}^{5} C_l e^{-\mu/T_\perp^l} e^{(W-\mu)/T_\parallel^l} \qquad (9)$$

where W is energy and μ is magnetic moment. The anisotropy factor $A \equiv T_\parallel/T_\perp$ is taken to be quite large, in the range 2–3. The value of perpendicular and parallel temperatures and coefficients C_l are given in Table 1. All the simulation runs will use a starting frequency of 3150 Hz, which is typical for the data.

4.1. Riser: Run A

The first simulation is of a long steady riser (Figure 2). The initial signal or trigger is a weak CW pulse of amplitude 0.3 pT (all amplitudes quoted are zero-to-peak) and length 86 ms. Note that in this code the trigger signal may be extremely small and the final emission is insensitive to the nature of the trigger. The equatorial electron plasma frequency is 175 kHz, and the initial electron resonance energy is about 2 keV. The linear electron cyclotron growth rate at the equator at 3150 Hz is taken to be 60 dB s^{-1}. This simulation uses a single pitch angle beam with pitch angle of 59° and $(N_{V_\perp} = 1)$. This pitch angle coincides with the sharp maximum of the quantity $F_0' V_\perp^2$. The phenomenological saturation level for this run is set at $B_{max} = 4.9$ pT, corresponding to a trapping frequency of 35 Hz. This level allows for about five trapping oscillations in the equatorial generation region, thus giving strongly nonlinear particle dynamics.

Observations of chorus at $L = 6$ taken on Geotail [*Nagano et al.*, 1996] showed very high wave amplitudes in the range 5–50 pT. Such observations suggest that the generation mechanisms of chorus and VLF emissions involve high levels of nonlinearity. Some simulations of VLF emission triggering at $L = 4$ have recently been performed with saturation amplitudes of ~9 pT. Very steep risers with sweep rates of ~2 kHz s^{-1} resulted. However, high-amplitude simulations are computationally extremely expensive to perform, and a more detailed investigation of this regime will be the subject of further work.

Table 1. Parameters for Distribution Function F_0

l	$T_\perp$, eV	$T_\parallel$, eV	C_l
1	25	25	1722
2	400	150	5.85
3	3,000	1,000	0.044
4	15,000	5,000	0.0009
5	50,000	20,000	0.00007

Figure 2 displays all the graphs for this run. The field values at the exit of the simulation box are fed into a delay line and subjected to overlapping block discrete Fourier transforms with Hamming weighting. Figure 2a is a frequency versus time plot in the form of a histogram-equalized shaded Interactive Data Language (IDL) contour plot of spectral power. A very stable and reproducible long-enduring riser is produced running up to 5 kHz with a sweep rate of about 1 kHz s^{-1}. This outcome is in good general agreement with observations. Figure 2b shows the B field exit amplitude as a function of time. The oscillations are clearly due to discrete sidebands allowed within the simulation bandwidth.

Figure 2c shows the amplitude profile in picoteslas in the simulation box at time $t = 877$ ms. The straight line shows the linear spatial variation of mean wave number, expressed as a frequency. This spatial variation is a significant factor in determining the overall frequency sweep rate of the emission. Figure 2e shows the corresponding plot of nonlinear resonant particle currents J_r and J_i, where J_r is the component parallel to $E_\perp$ and J_i is the component parallel to $B_\perp$. The form of these currents is exactly as expected from trapping in an inhomogeneous parabolically varying B field [see *Nunn*, 1986, 1990, 1993]. These two graphs define a stable quasi-static nonlinear structure, which we term a generation region (GR) or, more dubiously, a "VLF soliton". In the initial interaction phase the weak input signal grows exponentially in the linear regime. Once nonlinear wave amplitudes are reached in the equatorial zone, the stable GR structure is set up with an astonishing degree of repeatability. It is this GR that is the source of the emission. Since the GR structure has to stay in one position on the field line, a certain minimum linear growth rate must exist for a GR solution to be possible. At $L = 4.3$ this value is about 50 dB s^{-1}. Figure 2d plots the spatial gradient of wave number as a function of time, expressed as a sweep rate through

$$df/dt \sim V_g^2 dk/dz \qquad (10)$$

Clearly from the graph we can see that advection makes a highly significant contribution to emission sweep rate, particularly at the end of the emission. Figure 2f shows an IDL wire diagram for the quantity ΔW or integrated energy change, plotted as a function of gyrophase ψ and parallel velocity V_z, evaluated at the equator. The region of large positive ΔW demarcates the region of stable particle trapping. The VHS method is particularly effective for plasma diagnostics, in that

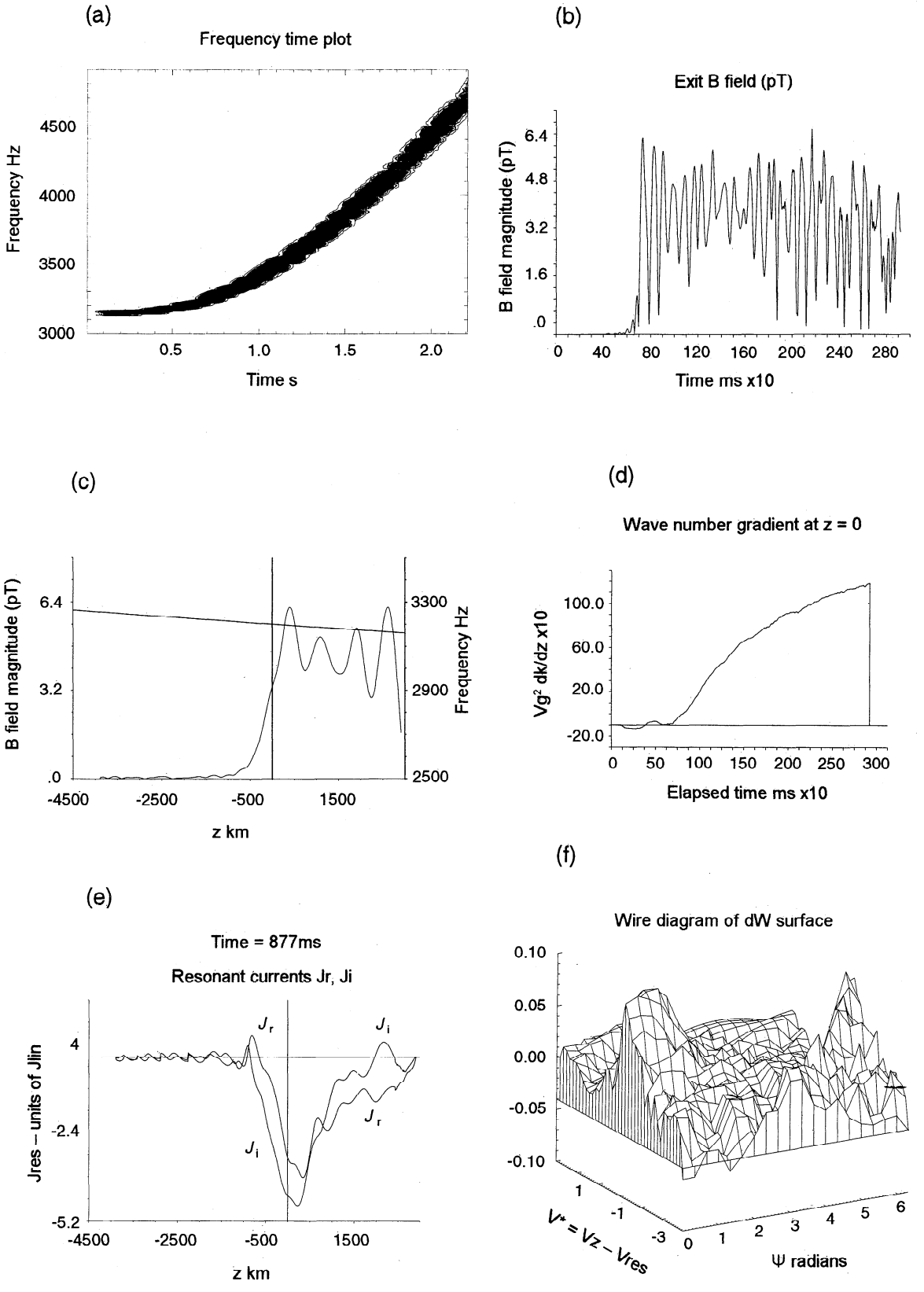

Figure 2. Output data from the numerical simulation of a rising frequency VLF emission, using a 1-D Vlasov VHS code. (a) The f–t spectrogram in the form of an IDL contour plot of spectral power. (b) Wave exit amplitude as a function of time. (c), (e) Structure of the GR at 877 ms. The vertical line is at the equator. (d) Spatial gradient of frequency in the GR as a function of time. (f) Plot of integrated energy change ΔW in the (V_z, ψ) plane at the equator.

individual particle trajectories are available simultaneously with any plots of distribution function as desired.

4.2. Faller: Run B

Figure 3 plots results for the simulation of a faller with a small upward hook at the end. The only parameter different from the riser case is the linear equatorial growth rate, now higher at 95 dB s^{-1}. The contour frequency versus time plot (Figure 3a) shows a faller down to 2500 Hz with a sweep rate of approximately -500 Hz s^{-1}, matching the faller in Figure 1b very well.

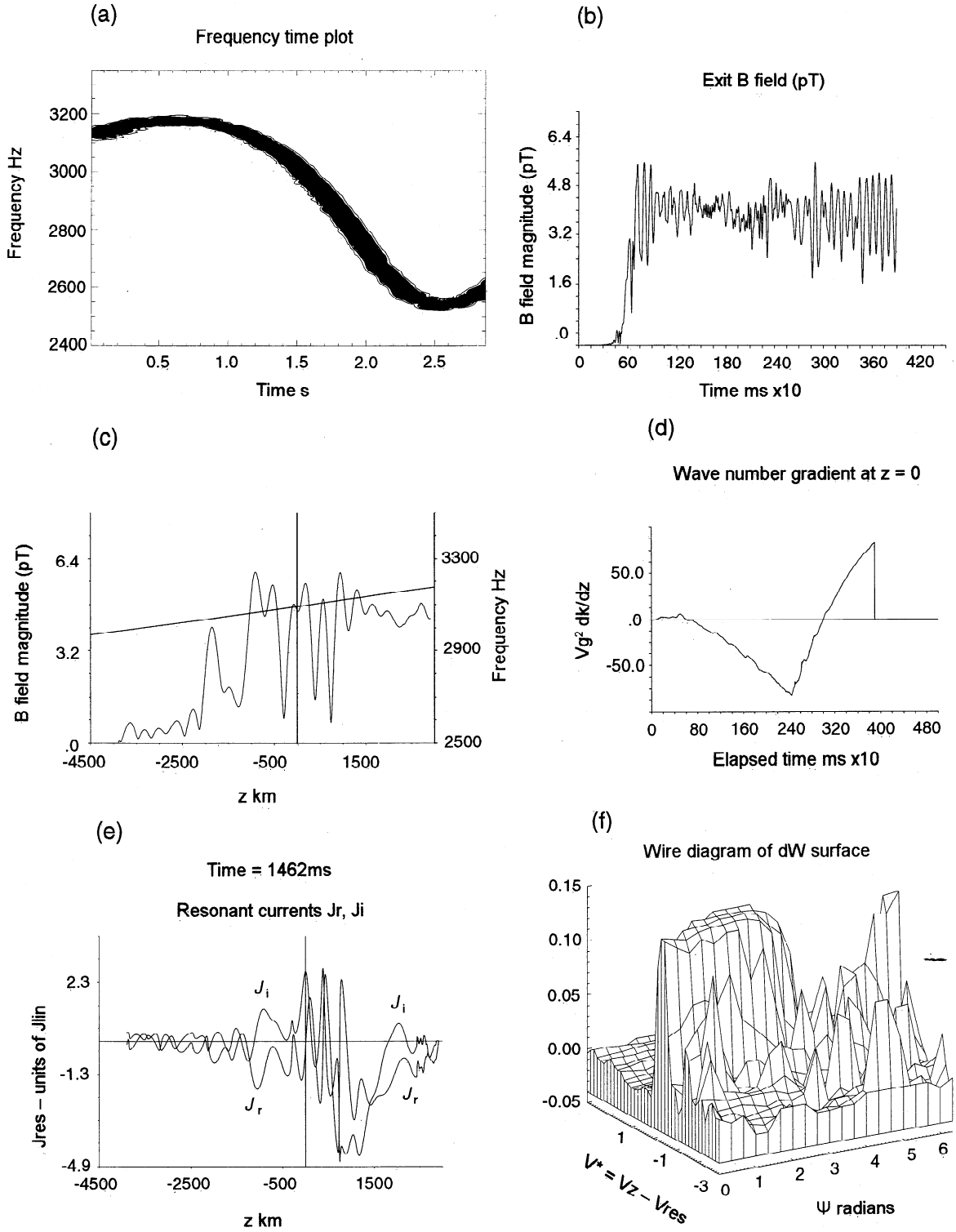

Figure 3. Output data from the numerical simulation of a falling frequency VLF emission, using a 1-D Vlasov VHS code. (a) The f–t spectrogram in the form of an IDL contour plot of spectral power. (b) Wave exit amplitude as a function of time. (c), (e) Structure of the GR at 1462 ms. (d) Spatial gradient of frequency in the GR as a function of time. (f) Plot of integrated energy change ΔW in the (V_z, ψ) plane at the equator.

However, elsewhere in the data, fallers are often very steep, with sweep rates as steep as -2 kHz s^{-1}.

The GR structure of the faller is shown in Figures 3c and 3e. It is clearly different from that of the riser. The amplitude profile extends well upstream from the equator, apparently as a result of the considerably increased growth rate. As a result, trapping takes place on the transmitter side of the equator, giving a positive value of J_i in this region [see *Nunn*, 1990, 1993]. The result is that $\Phi = d/dz(J_i/R)$ becomes negative, and a positive dk/dz gradient is set up across the GR (see Figure 3c). Hooks occur when the GR is destabilized in some way and spontaneously transforms itself from the riser type to the faller type or vice versa. For example, a loss of power input, such as might emanate from a fall in frequency, may cause a faller GR to slip downstream and become of the riser type. The result is an upward hook. This actually happens in this example at $t = 2.5$ s, as is evidenced in Figure 3d, where the spatial gradient dk/dz changes sign.

Figure 3f shows an IDL wire diagram of ΔW as a function of V_z and ψ at the equator. Not surprisingly, a bunch of stably trapped particles, marked by their large values of ΔW, are clearly visible. For a wave field with a bandwidth of $\sim$1 trapping frequency, the structure of the distribution function in velocity space is more complex than that predicted by simple trapping theory in the case of a CW wave.

4.3. Upward Hook: Run C

The third simulation is of an upward hook, the results being presented in Figure 4. This emission is triggered by a steady state hiss band infinitely extended in time, modeled by a large number (80) of sinusoids with random phase. The hiss band spectrum occupies the simulation bandwidth of 55 Hz in this case and has an RMS amplitude of 0.7 pT in this band. This code cannot model a true hiss band in view of the band-pass nature of the code's internal matched filter. The parameter settings for this simulation are otherwise the same as those for the previous two runs, except that the equatorial linear growth rate is 115 dB s^{-1} and the code is driven by a single $V_\perp$ beam with a pitch angle of 53.5°.

Figure 4a shows the f–t spectrogram for this hiss-triggered hook. There is an initial fall of 200 Hz within 0.6 s, followed by an upward hook and a strong riser with a sweep rate of about 700 Hz s^{-1}. Figures 4c and 4f, at $t = 573$ ms, show a GR of the classic faller type, with a wave profile extending upstream to $z = -3000$ km and a pronounced positive value for J_i upstream of the equator. By contrast, Figures 4d and 4e at $t = 2$ s show a GR with the characteristic structure of a riser. The amplitude profile is largely confined to the region downstream of the equator, and both J_r and J_i are negative, characteristic of trapping in regions of negative inhomogeneity. At $t = 1.7$ s the faller type GR transforms itself to a riser type. Again this effect is due to a loss of power input resulting from falling frequency, allowing the wave profile to slip downstream.

4.4. Downward Hook: Run D

The last computational run presented will be of a downward hook, the result being shown in Figure 5. The triggering signal is again a short CW pulse. The simulation parameters are identical to those of the first case (riser) except that the linear equatorial growth rate is 99 dB s^{-1}. The f–t diagram (Figure 5a) shows an initial segment rising to +200 Hz after about 1 s, then there is a gradual transformation to a steep faller with a slope of -600 Hz s^{-1}. Eventually, the faller terminates because the linear growth rate at these lower frequencies falls below the threshold level. Figures 5c and 5e at $t = 2.6$ s in the falling segment reveal the classic faller GR structure. The positive spatial gradient dk/dz in the GR is quite steep, giving a frequency variation across the GR of about 300 Hz. This is borne out by Figure 5d, which shows a frequency gradient initially small and positive becoming of the order of -1 kHz s^{-1} at the end of the emission.

Figure 5f shows an IDL shaded contour plot of ΔW in the (V_z, ψ) plane at the equator. Again the stably trapped particle bunch, characterized by large positive ΔW, dominates the topology of the distribution function in velocity space.

A theoretical question of some interest is what determines whether a riser or a faller is triggered. A comprehensive answer requires a very lengthy program of simulations in which each simulation parameter is varied in turn, i.e., input pulse length and amplitude, linear growth rate, saturation level B_{max}, and distribution function parameters. For the case of weak trigger signals that we have here, some idea of the dominant factors can be obtained. Strong linear growth rates seem to produce fallers, since the GR is set up upstream of the equator. Conversely, weaker growth rates result in a GR set up farther downstream, giving a riser. Also, provided linear growth rate falls monotonically with frequency, there will always be a tendency for risers to become fallers and fallers to become risers, because falling power input causes the wave profile to slip downstream and vice versa.

This effect is evident in the Halley data presented here, where both types of hooks are common. However, the process of triggering and establishing a stable GR is a highly complex and dynamic one, and it is difficult to parameterize in a simple way.

5. Conclusions

A search of the Halley VLF data base has revealed a rich variety of discrete and triggered VLF emissions.

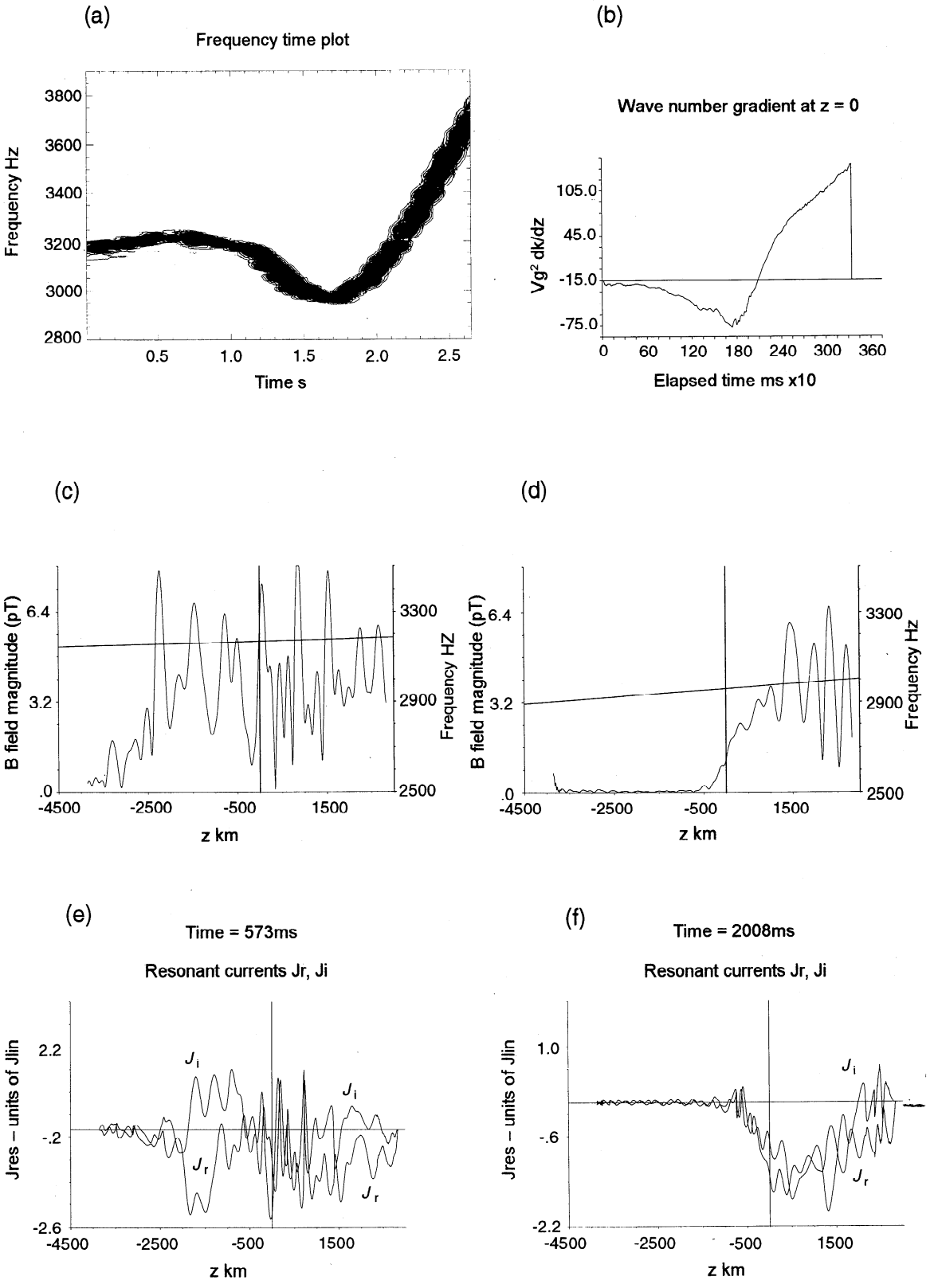

Figure 4. Output data from the numerical simulation of an upward hook VLF emission, using a 1-D Vlasov VHS code. (a) The f–t spectrogram in the form of an IDL contour plot of spectral power. (b) Wave exit amplitude as a function of time. (c), (e) Structure of the faller GR at 573 ms. (d), (f) Structure of the riser GR at $t = 2008$ ms.

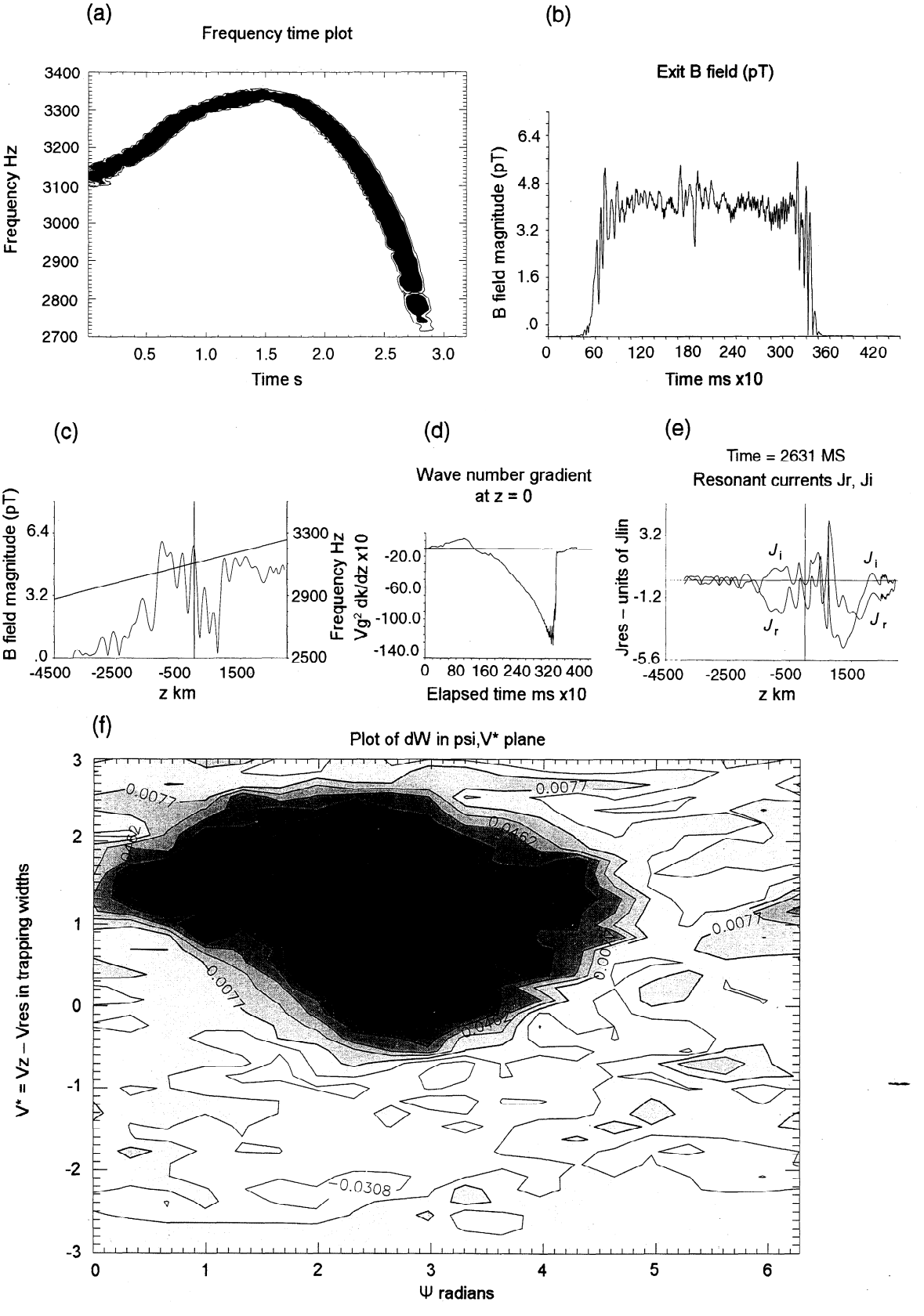

Figure 5. Output data from the numerical simulation of a downward hook VLF emission, using a 1-D Vlasov VHS code. (a) The f–t spectrogram in the form of an IDL contour plot of spectral power. (b) Wave exit amplitude as a function of time. (c), (e) Structure of the GR at 2631 ms. (d) Spatial gradient of frequency in the GR as a function of time. (f) Plot of integrated energy change ΔW in the (V_z, ψ) plane at the equator.

Risers, fallers, and upward and downward hooks are all quite common. Also the triggering of both risers and fallers from the top of a hiss band has been noted.

Using a 1-D Vlasov Hybrid Simulation code, we have simulated the main types of events observed, using plausible plasma parameters. Two key parameters are not directly available. The first is the linear cyclotron growth rate at the equator at the simulation starting frequency. It transpires that there is a minimum threshold growth rate in order for a generation region to be self-sustaining. In these simulations, provided linear growth rate is set above the threshold, satisfactory triggered emissions are produced, and the exact value for linear growth rate is not critical. The second parameter is the in-duct wave amplitude at the exit of the equatorial generation region. These simulations use a figure of the order of 5 pT, corresponding to several trapping oscillations by trapped cyclotron resonant electrons in their traversal of the generation region. Amplitudes of this order thus impart a significant level of nonlinearity, and the fact that the code readily simulates emissions as observed tends to confirm that nonlinear trapping is the root plasma physical mechanism behind triggered VLF emissions.

A remarkable feature of the code is that provided the linear growth rate exceeds the threshold level—here about 50 dB s^{-1}—the plasma effectively exhibits a nonlinear absolute instability. Any small initial trigger signal will undergo linear amplification at first and then develop a stable nonlinear GR soliton. The GR structure is very stable, and the setup process is eminently repeatable.

A significant result from running the code has been the insight it provides into GR structure. There are clearly two distinct structures: one for risers and the other for fallers. The riser GR is largely confined to downstream of the equator, while the faller GR extends well upstream from the equator. Hooks must result from a spontaneous transfer between these two quasi-stable forms.

The most unsatisfactory feature of the code is the need to employ an artificial saturation mechanism to prevent blowup of wave amplitude. We hypothesize that in reality, saturation must result from nonlinear unducting loss, and the 3-D simulation of such a process will remain unattainable for a while. Another aspect of the problem, currently unexplored, is the fact that nonlinear cyclotron resonant trapping will induce electrostatic instability, and the resultant plasma diffusion in the V_z direction will act to saturate whistler wave growth. This problem will be amenable to attack in the near future.

Last, the current code runs on a short timescale of the order of a few seconds. There is no recirculation of particles or fields after one bounce time. With a fairly acceptable increase in workload these aspects of the problem could be accommodated.

Acknowledgments. One author (D.N.) wishes to gratefully acknowledge the services of the Computing Service at Southampton University. In addition, thanks are due to the Radio Atmospheric Science Center at Kyoto University, Japan. Extensive code development took place on the KDK system during the tenure of a Visiting Professorship.

The Editor thanks two referees for their assistance in evaluating this paper.

References

Burtis, W. J., and R. A. Helliwell, Magnetospheric chorus: Occurrence patterns and normalized frequency, *Planet. Space Sci., 24,* 1007, 1976.

Carlson, C. R., R. A. Helliwell, and D. L. Carpenter, Variable frequency VLF signals in the magnetosphere: Associated phenomena and plasma diagnostics, *J. Geophys. Res., 90,* 1507, 1985.

Carlson, C. R., R. A. Helliwell, and U. S. Inan, Space-time evolution of whistler mode wave growth in the magnetosphere, *J. Geophys. Res., 95,* 15,073, 1990.

Cheng, C. Z., and G. Knorr, The integration of the Vlasov equation in configuration space, *J. Comput. Phys., 22,* 330, 1976.

Denavit, J., Numerical simulation of plasmas with periodic smoothing on phase space, *J. Comput. Phys., 9,* 75, 1972.

Helliwell, R. A., *Whistlers and Related Ionospheric Phenomena*, Stanford Univ. Press, Stanford, Calif., 1965.

Helliwell, R. A., A theory of discrete VLF emissions from the magnetosphere, *J. Geophys. Res., 72,* 4773, 1967.

Helliwell, R. A., Controlled stimulation of VLF emissions from Siple station, Antarctica, *Radio Sci., 18,* 801, 1983.

Helliwell, R. A., VLF wave stimulation experiments in the magnetosphere from Siple station, Antarctica, *Rev. Geophys., 26,* 551, 1988.

Helliwell, R. A., and J. P. Katsufrakis, VLF wave injection into the magnetosphere from Siple station, Antarctica, *J. Geophys. Res., 79,* 2511, 1974.

Nagano, I., S. Yagitani, H. Kojima, and H. Matsumoto, Analysis of wave normal and Poynting vectors of the chorus emissions observed on Geotail, *J. Geomagn. Geoelectr., 48,* 299, 1996.

Nunn, D., A nonlinear theory of sideband stability in ducted whistler mode waves, *Planet. Space Sci., 34,* 429, 1984.

Nunn, D., A quasi static theory of triggered VLF emissions, *Planet. Space Sci., 34,* 429, 1986.

Nunn, D., The numerical simulation of VLF nonlinear wave-particle interactions in collision-free plasmas using the Vlasov Hybrid Simulation technique, *Comput. Phys. Commun., 60,* 1, 1990.

Nunn, D., A novel technique for the numerical simulation of hot collision-free plasma: Vlasov Hybrid Simulation, *J. Comput. Phys., 108,* 180, 1993.

Nunn, D., and A. J. Smith, The numerical simulation of whistler-triggered emissions in Antarctica, *J. Geophys. Res., 101,* 5261, 1996.

Nunn, D., Y. Omura, H. Matsumoto, I. Nagano, and S. Yagitani, The numerical simulation of VLF chorus and discrete emissions observed on the Geotail satellite using a Vlasov code, *J. Geophys. Res., 102,* 27,083, 1997.

Omura, Y., and H. Matsumoto, Computer simulations of basic processes of coherent whistler wave-particle interactions in the magnetosphere, *J. Geophys. Res., 87,* 4435, 1982.

Omura, Y., and H. Matsumoto, Simulation study of frequency variations of VLF triggered emissions in a homogeneous field, *J. Geomagn. Geoelectr., 37,* 829, 1985.

Park, C. G., VLF wave activity during a magnetic storm: A case study of the role of power line radiation, *J. Geophys. Res., 82,* 3251, 1977.

Smith, A. J., VELOX: A new VLF/ELF receiver in Antarctica for the Global Geospace Science mission, *J. Atmos. Terr. Phys., 57,* 507, 1995.

Smith, A. J., P. Hughes, and K. H. Yearby, DSP-II and its applications: A unified approach to the acquisition and analysis of VLF radio wave data for research, *RadioScientist, 5(3),* 120, 1994.

Yearby, K. H., and A. J. Smith, The polarisation of whistlers received on the ground near $L = 4$, *J. Atmos. Terr. Phys., 56,* 1499, 1994.

D. Nunn, Department of Electronics and Computer Science, University of Southampton, Southampton, SO17 1BJ, England. (e-mail: D.Nunn@ecs.soton.ac.uk)

A. J. Smith, British Antarctic Survey, High Cross, Madingley Road, Cambridge, CB3 0ET, England. (e-mail: A.J.Smith@bas.ac.uk)

(Received May 16, 1997; revised November 10, 1997; accepted November 14, 1997.)